Research Article

Chao Feng, Rong Zhu*, Guangsheng Wei, Jianfeng Dong, and Kai Dong*

Jet characteristics of CO_2–O_2 mixed injection using a dual-parameter oxygen lance nozzle for different smelting periods

https://doi.org/10.1515/htmp-2021-0035
received June 14, 2021; accepted September 10, 2021

Abstract: The jet performance of an oxygen lance nozzle influences the smelting rhythm, smelting index, and energy consumption of a converter. Due to the complexity of the process of converter smelting, the changing temperature and gas composition in the converter significantly impact the jet characteristics of the oxygen lance nozzle in the smelting process; however, research on the change law of jet characteristics in different smelting periods is limited. In this study, we used Ansys Fluent 17.0, which is commercially available fluid simulation software, to simulate the variation of jet characteristics of a mixed injection comprising 6% CO_2 and 94% O_2; the mixed injection was tested using a dual-parameter oxygen lance nozzle in the early, middle, and late stages of smelting. The results show that the increase of CO concentration and ambient temperature in the converter lead to a decrease in the attenuation rate of jet velocity, improved independence of multiple jets, and an increase in the impact area of jets on the molten pool. Thus, when designing and employing oxygen lance nozzles, the influence of ambient temperature and furnace gas composition on jet characteristics must be considered.

Keywords: jet, furnace gas composition, ambient temperature, CO_2–O_2 mixed injection.

1 Introduction

The top and bottom combined blowing method is essential for the converter smelting process wherein an oxygen lance is the essential equipment for top blowing oxygen supply. The oxygen medium forms a supersonic jet through the oxygen lance nozzle to realize the oxygen supply and stirring of molten steel. The performance of the nozzle directly affects the converter smelting rhythm and smelting index. Therefore, it is crucial to study the supersonic jet characteristics of the nozzle [1–5].

Several researchers have conducted extensive research on the characteristics of a supersonic jet. The main methods employed in the studies include the cold hydraulic model, computer numerical simulation, and hot experiment [6–9]. The main research areas included nozzle parameters, nozzle layout, and environmental conditions. Lv and Zhu [10] studied the effect of the adjoint flow on the jet characteristics, and the results indicate that the increase of the adjoint flow velocity is beneficial to reduce the velocity attenuation of the main jet. Li et al. [11] studied the coalescence characteristics of supersonic jets from multinozzle lances under different conditions. The results show that the jets prefer to deviate from their own nozzle axes and tend to coalescence with the decreasing ambient temperature/nozzle inclination angle or increasing nozzle number. The attenuations of the velocity and dynamic pressure at the jet centerline are delayed with the increase of ambient temperature or the decrease of nozzle number/inclination angle. Zhang et al. [12] employed the hydraulic model to simulate the effect of a jet on converter splashing. The results of the study indicated that an increase in the gas supply flow changed

* **Corresponding author: Rong Zhu,** School of Metallurgical and Ecological Engineering, University of Science and Technology Beijing, Beijing 100083, China; Beijing Key Laboratory of Research Center of Special Melting and Preparation of High-end Metal Materials, University of Science and Technology Beijing, Beijing 100083, China, e-mail: zhurong1_1201@126.com
* **Corresponding author: Kai Dong,** School of Metallurgical and Ecological Engineering, University of Science and Technology Beijing, Beijing 100083, China; Beijing Key Laboratory of Research Center of Special Melting and Preparation of High-end Metal Materials, University of Science and Technology Beijing, Beijing 100083, China, e-mail: dongkaisteel@163.com
Chao Feng, Guangsheng Wei, Jianfeng Dong: School of Metallurgical and Ecological Engineering, University of Science and Technology Beijing, Beijing 100083, China; Beijing Key Laboratory of Research Center of Special Melting and Preparation of High-end Metal Materials, University of Science and Technology Beijing, Beijing 100083, China

the shape of the impact crater of the jet on the molten pool. Liu et al. [13] studied the change of Laval jet characteristics designed using a simplified Laval nozzle and a characteristic method. The Laval nozzle designed using this characteristic method exhibits improved jet characteristics and greater impact force under identical conditions. Hu et al. [14] studied the influence of oxygen preheating temperatures on jet characteristics and conducted experiments in a 75-ton electric arc furnace. An increase in the oxygen preheating temperature led to improvements in the jet characteristics and the ability of the jet to stir the converter molten pool. Yang et al. [15] studied the influence of temperature on the jet characteristics of a swirl nozzle; an increase in temperature increased the jet velocity and elongated core section. Similar results were obtained by Alam et al. [16] and Wei et al. [17] in their investigations. Garajau et al. [18] studied the influence of jet combustion on nozzle wear and jet characteristics. The jet characteristics worsened when the flow rate was lower than the design flow rate, and ablation occurred at the outlet of the nozzle. Yang et al. [19] employed the hydraulic model to simulate the jet characteristics of a staggered arrangement of nozzle holes. The staggered arrangement reduced the splash and increased the stirring effect of the jet on the molten pool. Zhao et al. [20] studied a supersonic combustion coherent jet using numerical simulation and experimental investigation; the combustion of the jet increased the length of the main oxygen jet.

Compared with the traditional oxygen jet characteristics, some scholars studied the influence of CO_2 injection on the jet characteristics and smelting effect [21–24]. Lv et al. [25] studied a new process of phosphorus removal by introducing a fraction of CO_2 into O_2 and conducted dephosphorization experiments in 30 and 300 t steelmaking converters. This new process of CO_2–O_2 mixed gas injection was found to be beneficial for the reduction of phosphorus content in molten steel, improvement of the distribution ratio of phosphorus, and reduction of the loss rate of slag and iron.

Researchers have studied the effects of different nozzle parameters, injection media, ambient temperatures, and layouts on supersonic jet characteristics and, thus, an optimized design was achieved. However, there are a few studies on the jet characteristics of a CO_2–O_2 supersonic jet paired with a dual-parameter oxygen lance nozzle for different smelting periods. The software, Ansys Fluent, was used in this study to simulate the change law of jet characteristics of such a CO_2–O_2 mixed gas injection paired with a dual-parameter nozzle for different smelting periods; the influence of environmental temperature and flue gas composition on the jet characteristics was analyzed. The main objective of our study is to provide theoretical research data for the industrial application of CO_2–O_2 mixed gas injection dual-parameter oxygen lance nozzle; furthermore, our study urges the consideration of gas composition in converters when designing the nozzle. Optimization of the parameters of the oxygen lance nozzle is crucial.

2 Mathematical model

2.1 Governing equations

The following assumptions are put forward in order to better meet the accuracy requirements of the simulation process:

(1) The flow in the nozzle is a three-dimensional steady compressible nonisothermal process.
(2) Gas is an ideal gas, and its molecular viscosity is a function of temperature.
(3) Ignoring the wall friction of the Laval nozzle, it is considered that the inner wall of the nozzle hole is smooth.

According to the above assumptions, the main governing equations of this study are the mass equation, momentum equation, and energy equation.

The equations are as follows (equations (1)–(6)) [15,26].

The mass conservation equation is expressed as follows:

$$\frac{\partial(\rho\mu_i)}{\partial x_i} = 0, \tag{1}$$

where μ_i is the ith direction's velocity, m·s^{-1}; $\rho = P/RT$, and ρ is the density of gas, kg·m^{-3}; P is the pressure, Pa; R is the universal gas constant, 8.314 J·(mol·K)$^{-1}$; and T is the absolute temperature, K.

The equation of momentum conservation is given as follows:

$$\frac{\partial(\rho\mu_i\mu_j)}{\partial x_j} = -\frac{\partial p}{\partial x_i} + \frac{\partial(\tau_{ij} - \rho\overline{\mu_i\mu_j})}{\partial x_j}, \tag{2}$$

$$\tau_{ij} = \mu\left(\frac{\partial\mu_j}{\partial x_i} + \frac{\partial\mu_i}{\partial x_j} - \frac{2\partial\mu_k}{3\partial x_k}\delta_{ij}\right), \tag{3}$$

where μ_j is the jth direction's velocity, m·s^{-1}; p is the pressure of the system, Pa; τ_{ij} is the viscous stress results due to molecular viscosity, Pa; and δ_{ij} is the Kronecker delta, if $i = j$ or if $i \neq j$, therefore $\delta_{ij} = 0$ or $\delta_{ij} = 1$.

The values of parameters μ are defined in accordance with Sutherland's viscosity:

$$\mu = 2.67 \times 10^{-6}\left(\frac{C_E}{C_l^2}\right)\sqrt{\frac{M}{T}}, \tag{4}$$

where μ is the molecular viscosity, Pa·s; M is the molecular weight (kg·kmol^{-1}) and is equal to 32.96 kg·kmol^{-1}; C_E and C_1 are the Lennard–Jones energy parameter (K) and Lennard–Jones characteristic length [Å], respectively, and C_E = 195.2 K and C_l = 3.941 Å.

The energy conservation equation is expressed as follows:

$$\frac{\partial(\rho E)}{\partial t} + \nabla\cdot[\vec{v}(\rho E + \rho)] = \nabla\cdot\left[k_{\text{eff}}\nabla T - \sum_j h_j\vec{J_j} + (\bar{\bar{\tau}}_{\text{eff}}\cdot\vec{v})\right] + S_h, \tag{5}$$

$$E = \sum_j\left[y_j\cdot\left(\int_{T_{\text{ref}}}^{T} c_{p,j}\mathrm{d}T\right)\right] - \frac{P}{\rho} + \frac{v^2}{2}, \tag{6}$$

where k_{eff} is the effective conductivity; $\vec{J_j}$ is the diffusion flux of species; S_h is the heat produced by chemical reactions and any other volumetric heat sources; y_j is the mass fraction of j; $c_{p,j}$ is the temperature-dependent constant pressure specific heat capacity of species j; and T_{ref} = 298.15 K.

2.2 Turbulence model

In this study, a modified k–ε two-equation turbulence model is used.

The turbulent kinetic energy equation k is expressed as follows:

$$\frac{\partial(\rho k)}{\partial t} + \frac{\partial(\rho k v_i)}{\partial x_i} = \frac{\partial}{\partial x_j}\left[\left(\mu + \frac{\mu_i}{\sigma x_i}\right)\cdot\frac{\partial k}{\partial x_i}\right] + G_k + G_b - \rho\varepsilon - Y_M + S_k, \tag{7}$$

where v_i is the fluid flow velocity in the direction i, m·s^{-1}; G_k is the turbulence energy generated by the laminar velocity gradient, J; Y_M is the fluctuation due to excessive diffusion of compressible turbulence, J; G_b is the turbulence energy generated by buoyancy, J; and μ_t is the turbulent viscosity, Pa·s.

The equation of turbulent viscosity is given as follows:

$$\mu_t = \rho C_\mu\frac{k^2}{\varepsilon^2}, \tag{8}$$

where C_μ is a constant and is equal to 0.09.

The equation of dissipation rate ε is given as follows:

$$\frac{\partial(\rho\varepsilon)}{\partial t} + \frac{\partial(\rho\varepsilon v_i)}{\partial x_i} = \frac{\partial}{\partial x_j}\left[\mu + \frac{\mu_t}{\sigma_\varepsilon}\cdot\frac{\partial\varepsilon}{\partial x_i}\right] + C_{1\varepsilon}\frac{\varepsilon}{k}(G_k + C_{3\varepsilon}G_b) - C_{1\varepsilon}\rho\frac{\varepsilon^2}{k} + S_\varepsilon, \tag{9}$$

where σ_k and σ_ε are, respectively, the turbulent Prandtl numbers of k and ε; S_k and S_ε are the defined source terms, J; and, in this study, $C_{1\varepsilon}$ = 1.6, $C_{2\varepsilon}$ = 1.92, $C_{3\varepsilon}$ = 0.8, C_μ = 0.09, σ_k = 1.0, and σ_ε = 1.3.

The equation of species conservation is given as follows [27]:

$$\frac{\partial}{\partial t}(\rho\zeta_j) + \nabla\cdot(\rho\vec{v}\zeta_j) = -\nabla\cdot\vec{J_j} + R_j, \tag{10}$$

$$\vec{J_j} = -\left(\rho D_{j,m} + \frac{\mu_t}{Sc_t}\right)\cdot\nabla\cdot\zeta_j - D_{T,j}\frac{\nabla T}{T}, \tag{11}$$

where ζ_j is the mass fraction of j; $\vec{J_j}$ is the diffusion flux of species j; R_j is the net rate of the jth species produced by chemical reactions; $D_{j,m}$ is the jth species mass diffusion coefficient, $D_{T,j}$ is the thermal diffusion coefficient, and Sc_t is the turbulent Schmidt number and equal to 0.7; and T is the ambient temperature, K.

The equation of the combustion model is given as follows. The eddy dissipation (ED) model was employed to study the effects of the composition of the ambient gas on the characteristics of the supersonic oxygen jet [28,29]. Within the ED model, the net rate of the production of species j is due to reaction r; $R_{j,r}$ means the molar rate of species j in reaction r and is given by the smaller of the two equations as follows:

$$R_{j,r} = v'_{j,r}M_{\omega,j}A\rho\frac{\varepsilon}{\kappa}\min_R\left(\frac{\zeta_R}{v'_{j,r}M_{\omega,R}}\right), \tag{12}$$

$$R_{j,r} = v'_{j,r}M_{\omega,j}AB\frac{\varepsilon}{\kappa}\left(\frac{\sum_P\zeta_P}{\sum_i^N v''_{i,r}M_{\omega,i}}\right), \tag{13}$$

where $v'_{j,r}$ and $v''_{i,r}$ are the stoichiometric coefficient for reactant j and product j in reaction r, respectively; $M_{\omega,j}$, A, and B are the molecular weights of species j and empirical constants, respectively; κ and ε are the kinetic energy of the turbulence and the dissipation rate, respectively; and ζ_P and ζ_R are the mass fractions of any product species P and a particular reactant R, respectively.

The equation of the discrete ordinate (DO) radiation model is given as follows.

The DO radiation model was used and applied with the weighted sum of the gray gas model to obtain the

results of the combustion experiment [27]. The radiative transfer equation for absorbing, emitting, and scattering mediums at position $\rightarrow r$ in the direction $\rightarrow s$ is presented below:

$$\nabla\cdot[I(\vec{\gamma},\vec{s})\vec{s}] + (a+\sigma_s)I(\vec{\gamma},\vec{s}) = an^2\frac{\sigma T^4}{\pi} + \frac{\sigma_s}{4\pi}\int_0^{4\pi} I(\vec{\gamma},\vec{s}\,')\Phi(\vec{s},\vec{s}\,')\mathrm{d}\Omega', \quad (14)$$

where $\vec{\gamma}$ is the position; $\vec{s}$ is the direction vectors; $\vec{s}\,'$ is the scattering direction vector; s is the path length; n is the refractive index; a is the absorption coefficient, $\mathrm{L\cdot mol^{-1}\cdot cm^{-1}}$; n, σ_s, and σ are the refractive index, the scattering coefficient, and the Stefan-Boltzmann constant, respectively; I and T are the radiation intensity and local temperature; and Φ and Ω' are the phase fraction and the solid angle.

2.3 Computational domain and boundary conditions

In this study, the outer circle diameter of the dual-parameter oxygen lance nozzle was 406 mm, the design flow rate was 70,000 $\mathrm{N\cdot m^3\cdot h^{-1}}$, and a dual-parameter staggered nozzle design was adopted, which was suitable for 260–350 t converter smelting. The details of the parameters and simulation conditions of the nozzle are listed in Table 1. The large nozzle is represented by B and the small nozzle is represented by S. Figure 1 illustrates the structure of the nozzle. The nozzle has three large and three small holes. The throat diameters of the small and large holes are Dt_1 and Dt_2, respectively; the outlet diameters are De_1 and De_2, respectively; the angle between the nozzle and the nozzle centerline is given by α_1 and α_2, respectively; and the expansion angle of the nozzle is given by α_3 and α_4, respectively. The injected gas medium is a mixture of CO_2 and O_2.

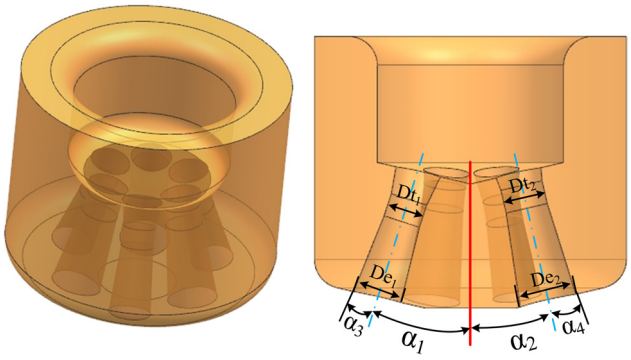

Figure 1: Nozzle structure.

We used ANSYS ICEM to mesh the hexahedron of the model. The total number of grids is 494,300 and the number of nodes is 506,316. ANSYS FLUENT 17.0 was used for CFD simulation. The computational domain is a cylindrical region with De_1 = 75 mm and De_2 = 55 mm. Figure 2 shows the computational domain and boundary conditions used in the simulation. The nozzle inlet was set as the mass flow inlet, the nozzle outlet as the pressure boundary outlet, and the nozzle wall and end face as the wall. The numerical simulation was based on the pressure-based solver, wherein the pressure velocity coupling equation is solved by the coupling algorithm (coupling algorithm). The density, momentum, turbulent kinetic energy, turbulent dissipation rate, and energy were solved using the second-order upwind scheme, and the implicit method was used, The reflux temperature is set to 1,873 K. The residual error of energy was less than 10^{-6}, and that of other variables was less than 10^{-5}, which was the convergence condition.

3 Model validation

To verify the validity of the research grid and mathematical model, a cold high-pressure jet detection system was adopted. The system flow chart, shown in Figure 3,

Table 1: Main technical parameters

Parameters	B	S	Ambient temperature (K)	1,673		
Number of holes	3	3		1,823		
Dt_1/Dt_2 (mm)	54.5	47.8		1,923		
De_1/De_2 (mm)	73.7	62.3	Gas medium	94% O_2 + 6% CO_2		
α_1/α_2 (deg)	18.5	12.5	Gas composition	Prophase (%)	Metaphase (%)	Anaphase (%)
α_3/α_4 (deg)	4.5	4	CO	35	76	55
Mach number	2.09	2.01	CO_2	65	24	45
Flow rate ($\mathrm{N\cdot m^3\cdot h^{-1}}$)	70,000		Molar mass ($\mathrm{g\cdot mol^{-1}}$)	38.4	31.8	35.2

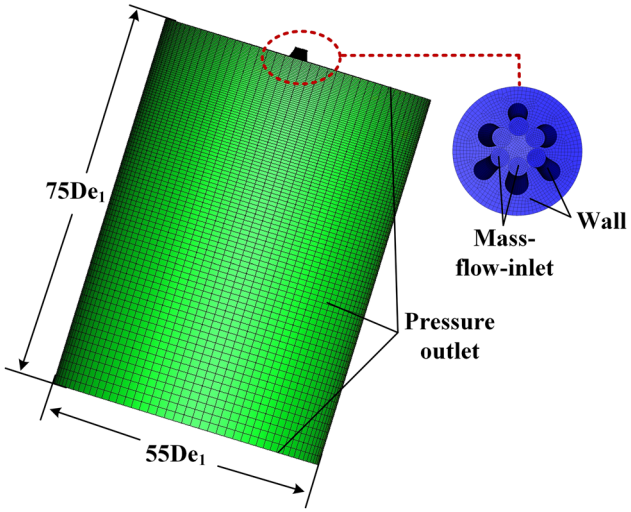

Figure 2: Calculation of the domain structure and the boundary setting of the dual-parameter oxygen lance nozzle.

comprises a high-pressure gas system, valve group control system, jet acquisition system, and data processing system. The high-pressure gas system can supply high-pressure gas greater than 1.5 MPa; this pressure is adjusted by the valve group control system to the pressure required by the test nozzle. The supersonic jet flows through the jet acquisition system and records the pressure of the jet; subsequently, it converts the pressure and digital signals using the data processing system. The internal model of the cold high-pressure jet detection system is shown in formulae (15)–(17):

$$v_e = \mathrm{Ma} \times a = \mathrm{Ma} \times \sqrt{\kappa RT}, \tag{15}$$

$$\frac{P_{0a}}{P_b} = \frac{\left(\frac{\kappa+1}{2}\mathrm{Ma}^2\right)^{\frac{\kappa}{\kappa-1}}}{\left(\frac{2\kappa}{\kappa+1}\mathrm{Ma}^2 - \frac{\kappa-1}{\kappa+1}\right)^{\frac{1}{\kappa-1}}}, \tag{16}$$

$$\frac{T}{T_a} = \frac{1}{1 + r\frac{\kappa+1}{2}\mathrm{Ma}^2}, \tag{17}$$

where T and T_a are jet temperature and measured temperature, respectively; Ma, v_e, and a are Mach number, jet exit velocity, and the calculated sound velocity; P_b and P_{0a} are the static pressure and the total pressure, Pa; r and κ are the transform coefficients of the kinetic energy to enthalpy and the adiabatic exponent.

In this study, the air supply flow rates were set at 70,000 and 80,000 $\mathrm{N{\cdot}m^3{\cdot}h^{-1}}$, and a processed test nozzle was used for testing. Prior to the test, the group of large and small holes on the nozzle was adjusted such that they were horizontal. During the test, the pressure acquisition row of the jet acquisition system was adjusted. The jet velocity values at 0.4, 0.6, 0.8, and 1.0 m away from the nozzle outlet were measured. Four groups of data were repeated at each position, and the average value and the standard deviation were calculated. The test results are shown in Figure 4. The results indicate that the numerical simulation results are similar to the cold test results; the maximum and minimum errors are 13.2 and 2.32%, respectively. The numerical simulation results and the experimental results are consistent.

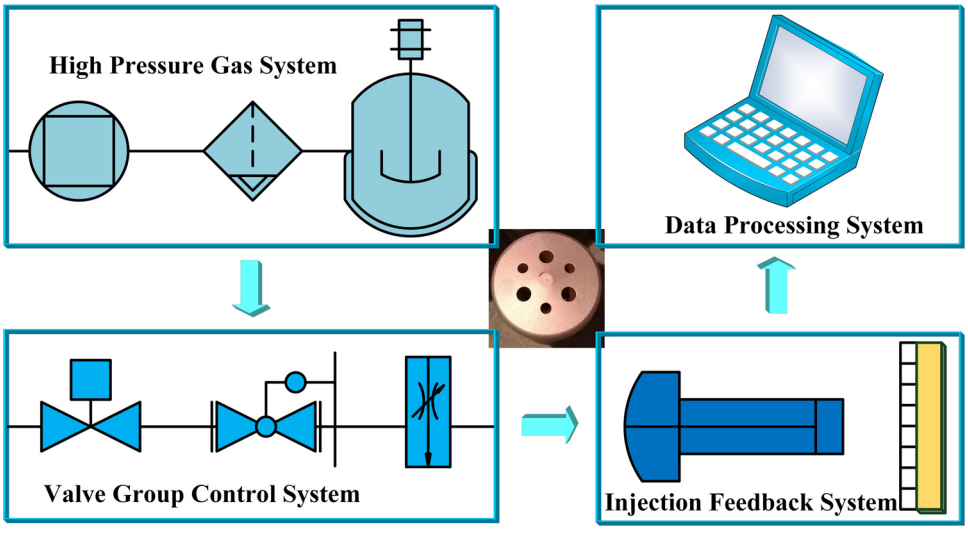

Figure 3: Cold high-pressure jet detection system.

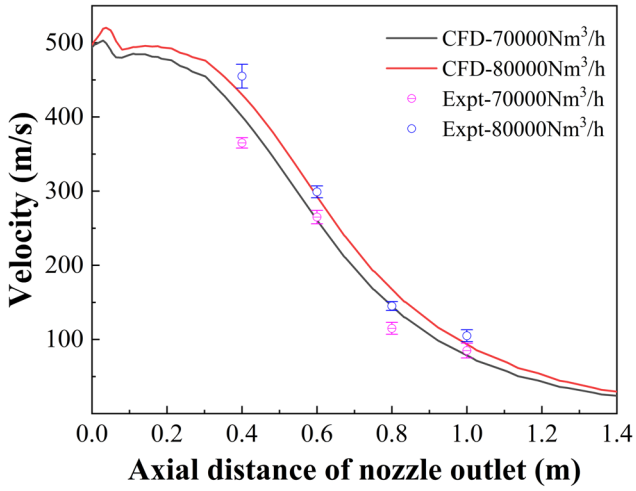

Figure 4: Comparison and verification of jet velocity distribution along the nozzle axis.

4 Results and discussion

The converter smelting process is affected by several factors, including hot metal temperature and composition as well as molten steel composition at the end of smelting. Therefore, three cases were considered: identical furnace gas composition, different converter temperatures; identical converter temperature, different furnace gas compositions; and different furnace gas compositions, different furnace gas temperatures. Furthermore, an analysis of jet characteristics under different actual production conditions was conducted. Three furnace gas compositions and three different ambient temperatures were applied. The influences of different conditions on the jet characteristics such as nozzle axis, jet radial distribution at different distances, and jet temperature distribution were analyzed. Furthermore, the influences of ambient temperature and furnace gas composition on the jet characteristics of CO_2–O_2 mixed gas injection with a dual-parameter oxygen lance nozzle in an actual converter smelting process were determined.

4.1 Influence of the same furnace gas composition and different ambient temperatures on jet characteristics

The influence of different ambient temperatures on the jet characteristics of the nozzle in the middle stage of

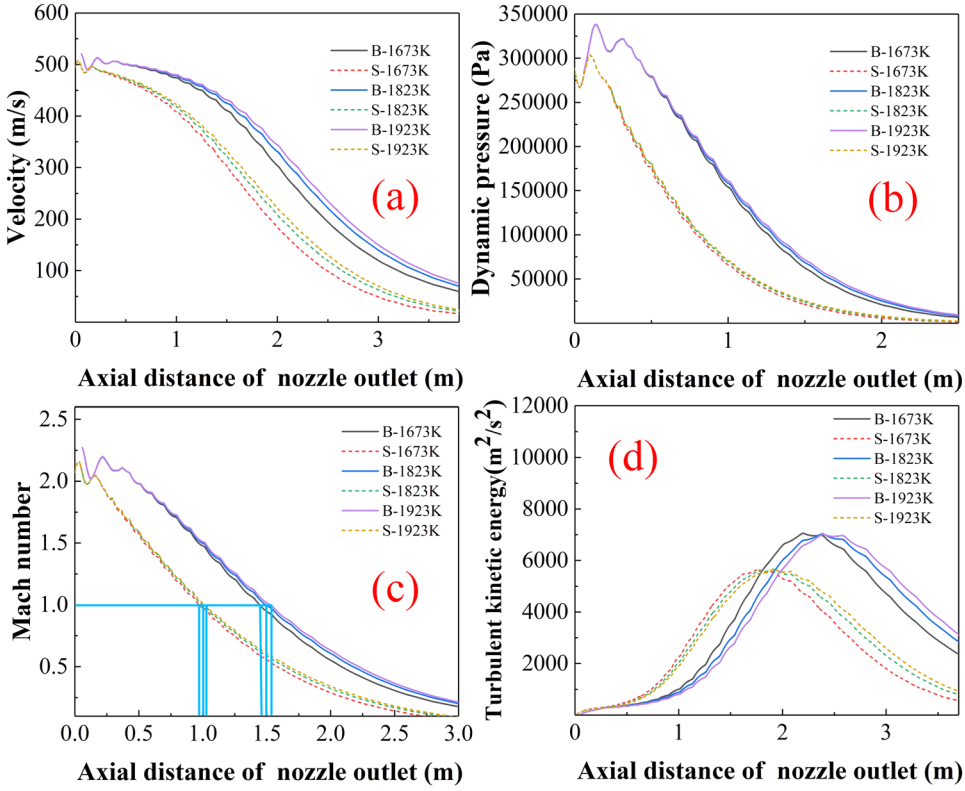

Figure 5: Jet characteristics of the nozzle axis at different ambient temperatures: (a) velocity, (b) dynamic pressure, (c) Mach number, and (d) turbulent kinetic energy.

converter smelting was simulated. The gas composition in the converter was set at 76% CO gas and 24% CO_2 gas, and the temperature in the converter was set to 1,673, 1,823, and 1,923 K. The change law of the jet under the conditions of low, normal, and high temperature in the actual smelting process of the converter was analyzed.

4.1.1 Axial jet of the nozzle orifice

Figure 5 shows the change law of the jet axis of the oxygen lance nozzle for different ambient temperatures. Under identical furnace gas compositions, an increase in the temperature in the converter leads to increases in the jet axial velocities of nozzles B and S, and the length of the core section of the jet. As shown in Figure 5(a) and (c), an increase in the injection distance results in a gradual decrease in the jet velocity, and the jet velocity of nozzles B and S follow a similar trend; however, the jet velocity of nozzle B is consistently greater than that of nozzle S. In accordance with the law of conservation of mass and energy, the jet exhibits higher velocity, slower jet attenuation, and longer core length; refer Figure 5(b) and equations (15), (18), and (19) for an explanation. The Mach number of nozzle B is larger than that of nozzle S; therefore, the jet velocity at the outlet of nozzle S is higher. Because the jet stream of nozzle S has a smaller diameter than that of nozzle B, the entrainment of gas has a greater influence on nozzle S and the jet attenuation is accelerated. The change law of the jet turbulent kinetic energy shown in Figure 5(d) can be used to explain the higher jet velocity of nozzle B than that of nozzle S:

$$\frac{\rho}{\rho_0} = \left(1 + \frac{(\kappa - 1)M^2}{2}\right)^{-\frac{1}{\kappa-1}} = \frac{T}{T_0}^{\left(\frac{1}{\kappa-1}\right)}, \tag{18}$$

$$v_e = \sqrt{2 \times \frac{\kappa g R(T_0 - T)}{\kappa - 1}}. \tag{19}$$

4.1.2 Axial jet of the oxygen lance nozzle

The jet characteristics of the nozzle axis can be used to measure the coalescence characteristics of multiple jet nozzles. Figure 6 shows the variation of jet characteristics of the nozzle axis with ambient temperature. The results indicate that the jet velocity, dynamic pressure, and Mach number decrease with an increase in the ambient

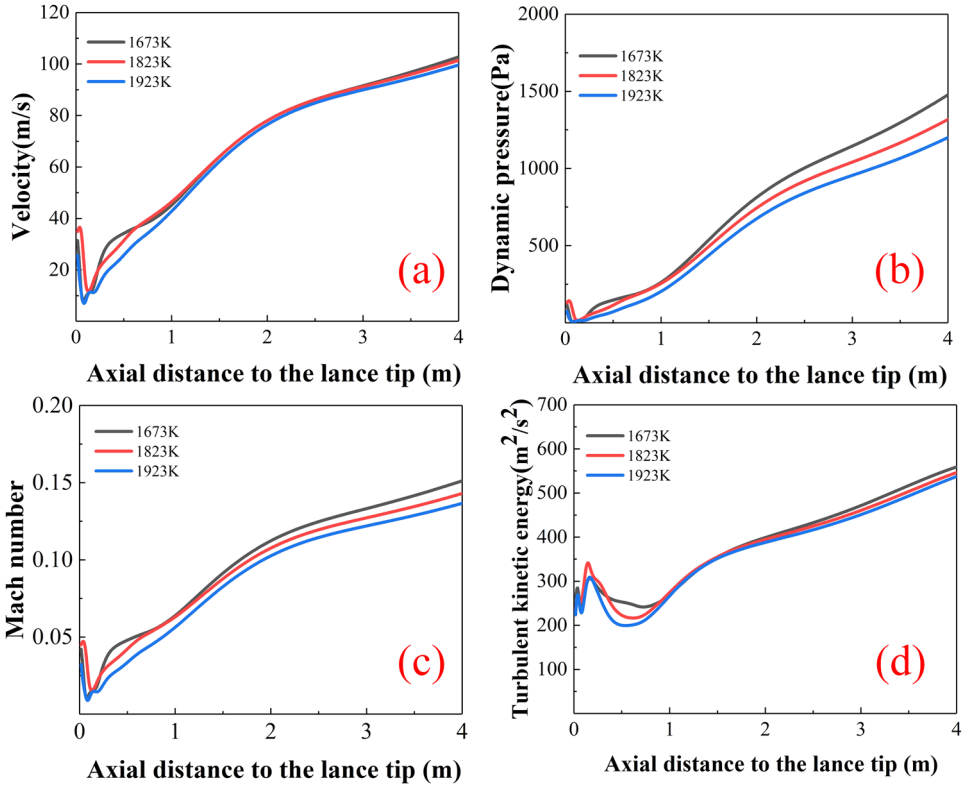

Figure 6: Jet characteristics of the nozzle centerline under different ambient temperatures: (a) velocity, (b) dynamic pressure, (c) Mach number, and (d) turbulent kinetic energy.

temperature at identical injection distances. Furthermore, there was an increase in the axial velocity, dynamic pressure, Mach number, and turbulent kinetic energy corresponding to an increase in the injection distance. The results obtained, as shown in Figure 6, are mainly due to the entrainment of ambient gas by multiple jets. The gas in the nozzle axis is unable to meet the entrainment of multiple jets, resulting in the mutual attraction and coalescence of multiple jets. Figure 5 illustrates that, with the increase in the ambient temperature, the jet velocity along the nozzle axis increases; the jet exhibits improved independence; the mixing of multiple jets decreases; and the velocity along the nozzle axis decreases. Furthermore, the change law of velocity and Mach number on the nozzle axis, as shown in Figure 6(a) and (c), can explain the reason for the decrease in the coalescence degree of the jet with an increase in the ambient temperature.

4.1.3 Radial distribution of jet

Figure 7 shows the distribution of jet characteristics at different injection distances with variations in the ambient temperature. The results indicate that under the same injection distance, with an increase in the ambient temperature, the maximum velocity of the jet axis of nozzles B and S increases, and the maximum velocity of the jet moves away from the axis of the nozzle; furthermore, the distance between the maximum velocity of nozzle B and the axis of the nozzle is consistently less than that of nozzle S. The results indicate that the maximum jet velocity decreases with an increase in the injection distance at identical ambient temperatures. The results shown in Figure 5(a) can be used to explain the distribution law of the jet as shown in Figure 7. With an increase in the ambient temperature, the attenuation rate of the jet velocity decreases; the jet velocity at an identical position increases; the opposition of the jet is improved; and the mixing degree of multi-jets is weakened. Therefore, with an increase in the ambient temperature, the distance between the maximum jet velocity point and the nozzle axis as well as the distance along the nozzle axis increase. The entrainment of ambient gas causes a gradual decrease in jet velocity.

Figure 8 shows the radial temperature distribution of the jet at different injection distances with an increase in the ambient temperature. The results indicate that at identical injection distances, as the ambient temperature increases, the temperature of the outside of the jet of nozzles B and S remains higher than that of the inside of the jet, and that of the side near the nozzle axis remains lower than that of the opposite side. Furthermore, the results indicate that with an increase in the injection

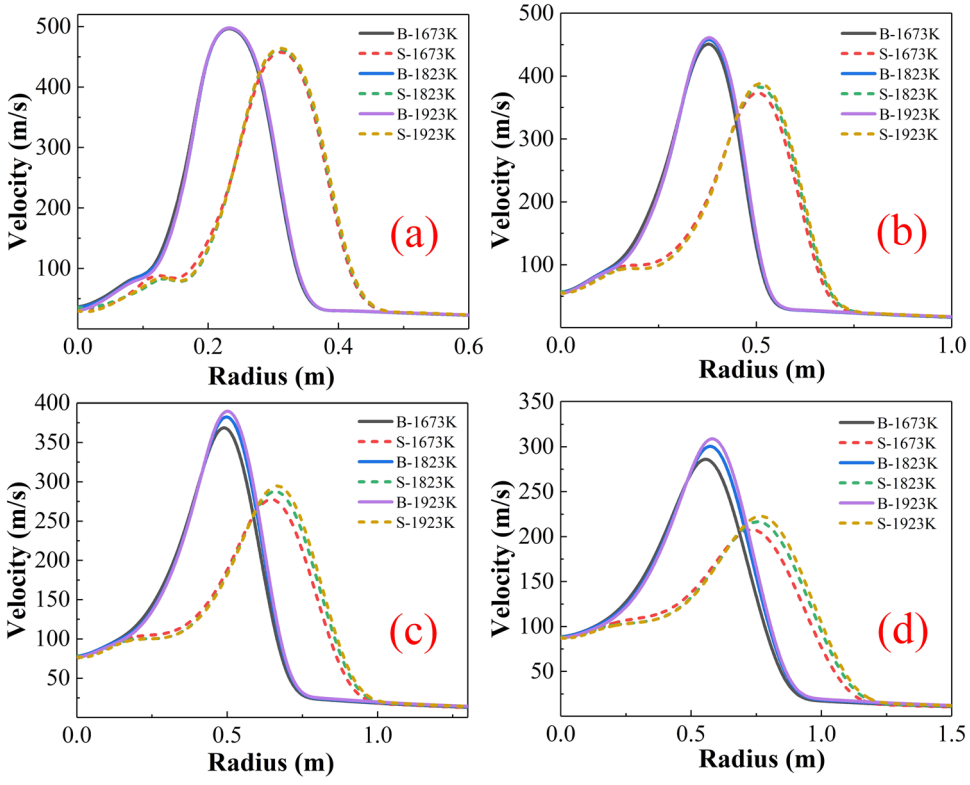

Figure 7: Radial velocity distribution of the jet at different temperatures: (a) 600 mm, (b) 1,300 mm, (c) 2,000 mm, and (d) 2,700 mm.

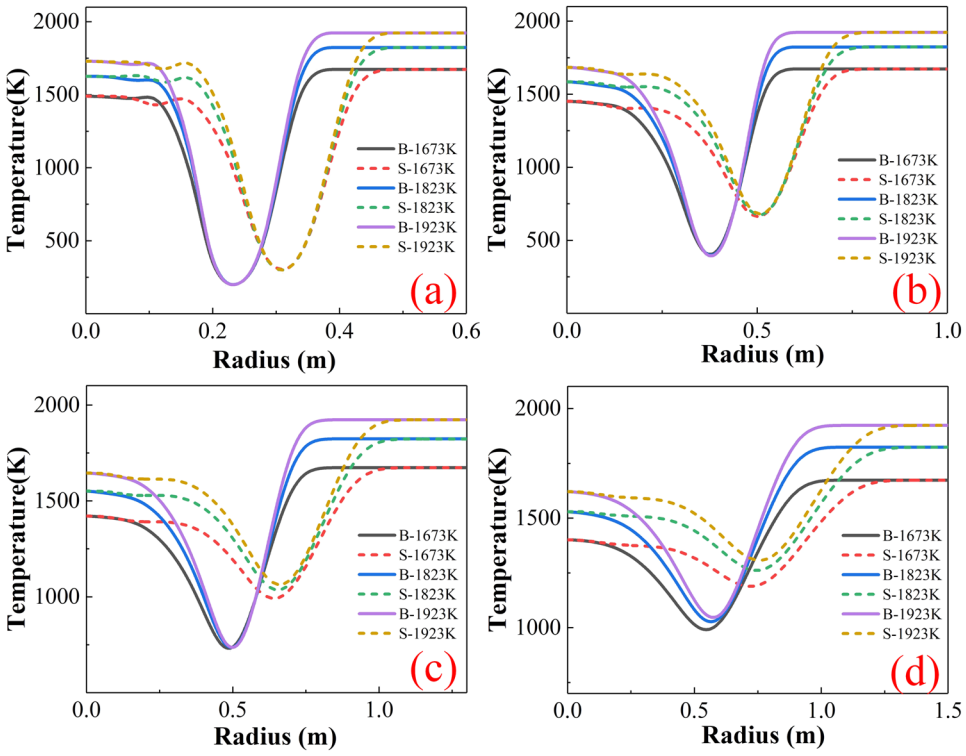

Figure 8: Radial temperature distribution of the jet under different temperature conditions: (a) 600 mm, (b) 1,300 mm, (c) 2,000 mm, and (d) 2,700 mm.

distance, the temperature difference between the jet near the nozzle axis and the opposite side increases; as the temperature decreases, the radial temperature distribution of the jet becomes smoother. The results shown in Figure 8 can be explained based on the results shown in Figure 5. The results shown in Figure 5(c) indicate that at injection distances of 600 and 1,300 mm, the jet of nozzle B remains supersonic; the convergence degree of multiple jets remains small, and the temperature on the nozzle axis is similar to the ambient temperature. With an increase in the injection distance, multijet coalescence occurs. At a lower ambient temperature, the degree of coalescence increases; consequently, the exchange degree between the jet and ambient gas increases, lowering the radial temperature near the nozzle axis side; thus, the radial temperature distribution becomes smoother.

4.2 Influence of different furnace gas compositions on jet characteristics at the same ambient temperature

The combustion reaction between the O_2 jet and the furnace gas is simulated at identical ambient temperatures, and the influence of the furnace gas composition on jet characteristics after combustion is analyzed. When the ambient temperature is 1,673 K, the composition of the furnace gas is 35% CO and 65% CO_2 in the early stage of smelting; 76% CO and 24% CO_2 in the middle stage of smelting; and 55% CO concentration and 45% CO_2 in the late stage of smelting. Thus, the characteristics of the CO_2–O_2 mixed jet combustion in different smelting periods are obtained.

4.2.1 Axial jet of the nozzle orifice

Figure 9 shows the effect of different furnace gas compositions on the jet characteristics of the nozzle axis at an ambient temperature of 1,673 K. The results show that the jet velocity of the nozzle jet is the highest in the middle stage of smelting and the lowest in the later stage of smelting, which indicates that the increase in the CO concentration in the furnace gas leads to an increase in the jet velocity of the nozzle axis. At the same ambient temperature, the CO and O_2 jets in the furnace gas burn, which leads to an increase in the ambient temperature around the jet. The results shown in Figure 5 indicate that the increase in the ambient temperature is beneficial to slow down the decay rate of the jet and extend the length of the core section of the jet.

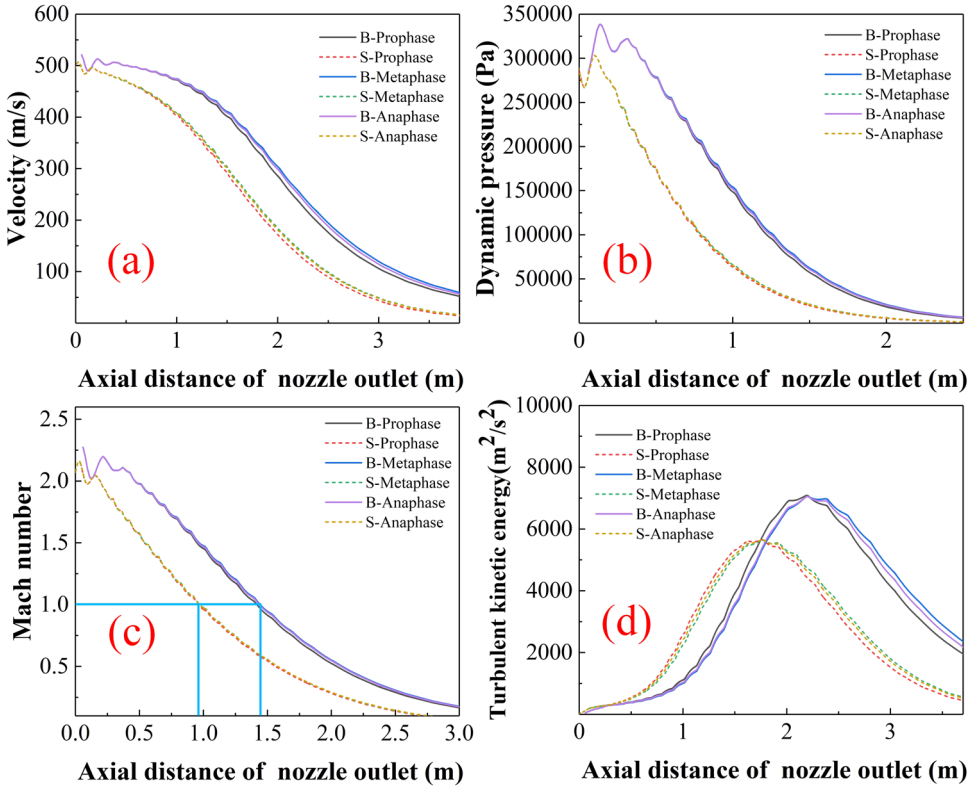

Figure 9: Jet characteristics of the nozzle axis under different atmosphere conditions: (a) velocity, (b) dynamic pressure, (c) Mach number, and (d) turbulent kinetic energy.

4.2.2 Axial jet of the oxygen lance nozzle

Figure 10 shows the distribution of jet characteristics along the nozzle axis under different furnace gas compositions. The results show that with the increase in the CO concentration in the furnace gas, the dynamic pressure and Mach number of the nozzle axis increase. The results shown in Figure 10 are mainly due to the increase of CO concentration, which is conducive to the combustion of the O_2 jet and slows down the attenuation of the jet. The independence of the jet is better, and the coalescence of multiple jets is weakened. Therefore, a lower CO concentration in the furnace gas led to a stronger coalescence of the jet.

4.2.3 Radial distribution of the jet

Figure 11 shows the radial distribution of jet characteristics under different furnace gas compositions. The results show that at the same distance, with the increase in CO concentration in the furnace gas, the maximum velocity of the jet increases; the distance between the maximum velocity point and the nozzle axis increases, and the jet offset phenomenon weakens. The result shown in Figure 11 is similar to that shown in Figure 7, mainly because the increase in CO concentration in the furnace gas increases the ambient temperature, slows down the attenuation of the jet velocity, and increases the jet velocity.

4.3 Change in nozzle jet characteristics in different smelting periods

The characteristics of the mixed injection CO_2–O_2 jet were studied under the following conditions: 1,673 K in the early stage of converter smelting, 35% CO and 65% CO_2 in the furnace gas, 1,823 K in the middle stage, 76% CO and 24% CO_2 in the furnace gas, 1,923 K in the late stage, and 55% CO and 45% CO_2 in the furnace gas.

4.3.1 Axial jet of the nozzle orifice

Figure 12 shows the distribution of jet characteristics along the nozzle axis in different smelting periods. The results indicate that nozzle B and nozzle S exhibit an increasing trend with an increase in the ambient

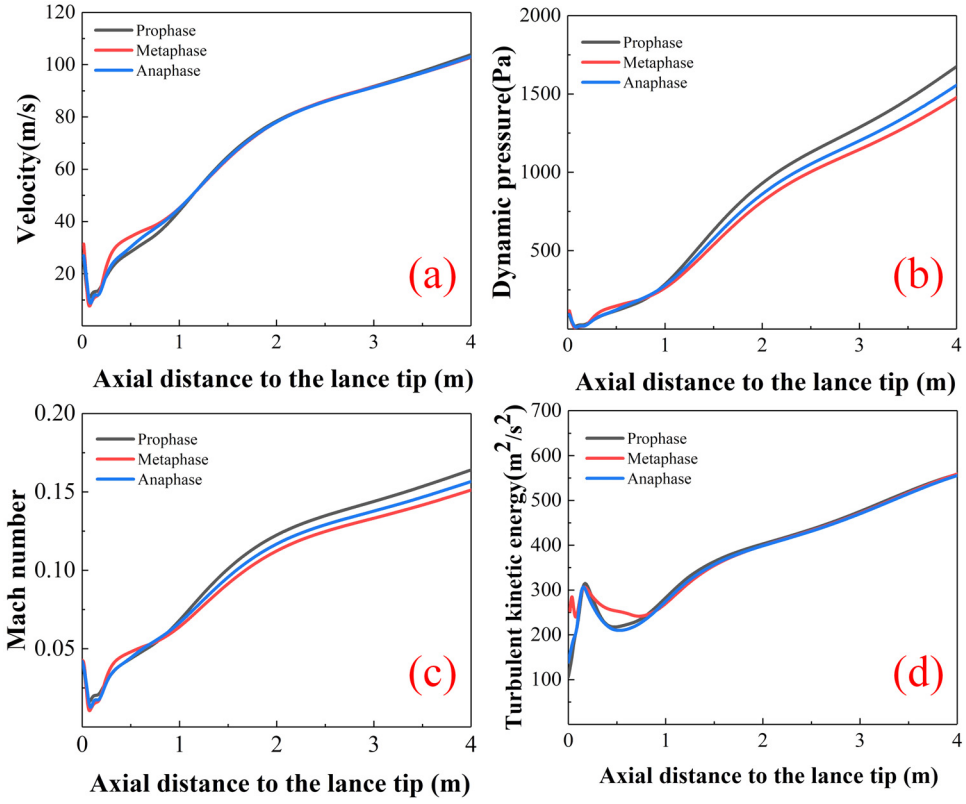

Figure 10: Jet characteristics of the nozzle centerline under different atmosphere conditions: (a) velocity, (b) dynamic pressure, (c) Mach number, and (d) turbulent kinetic energy.

temperature and CO concentration in the furnace gas. An increase in the CO concentration in the furnace gas and ambient temperature leads to an increased jet velocity and elongated jet core length. The results shown in Figure 12 can be analyzed based on the results shown in Figure 5. With the increase in the CO content in the furnace gas, the ambient temperature around the jet increases; therefore, the jet velocity attenuation slows down, and the length of the jet core section increases.

4.3.2 Axial jet of the oxygen lance nozzle

Figure 13 shows the jet characteristics distribution of nozzle centerline in different smelting periods. The results indicate that the dynamic pressure and Mach number on the nozzle axis increase with the increase in the ambient temperature and CO concentration in the converter gas, and the jet characteristics distribution is similar in the middle and late smelting stages. The results shown in Figure 13 can be explained as follows. As the CO concentration in the furnace gas increases, the temperature around the jet increases; the jet velocity is relatively larger, and the jet independence improves; therefore, the mixing degree of multiple jets is weakened. In the later stage of smelting, although the CO concentration in the furnace gas decreases, the increase in the ambient temperature also slows down the attenuation of jet velocity, and the independence of multiple jets is relatively better.

4.3.3 Radial distribution of the jet

Figure 14 shows the radial distribution of jet characteristics in different smelting periods. The results indicate that the maximum values of jet velocity in the middle and late stages of smelting are similar, which are greater than the maximum values of jet velocity in the early stage of smelting; furthermore, the jet deviations in the middle and late stages of smelting are similar, which are less than the jet offset in the early stage of smelting. With the increase in the injection distance, the jet velocities of nozzle B and nozzle S show a decreasing trend. The results shown in Figure 14 can be explained based on the results shown in Figure 12(a). The higher CO concentration in the furnace gas in the middle stage of smelting

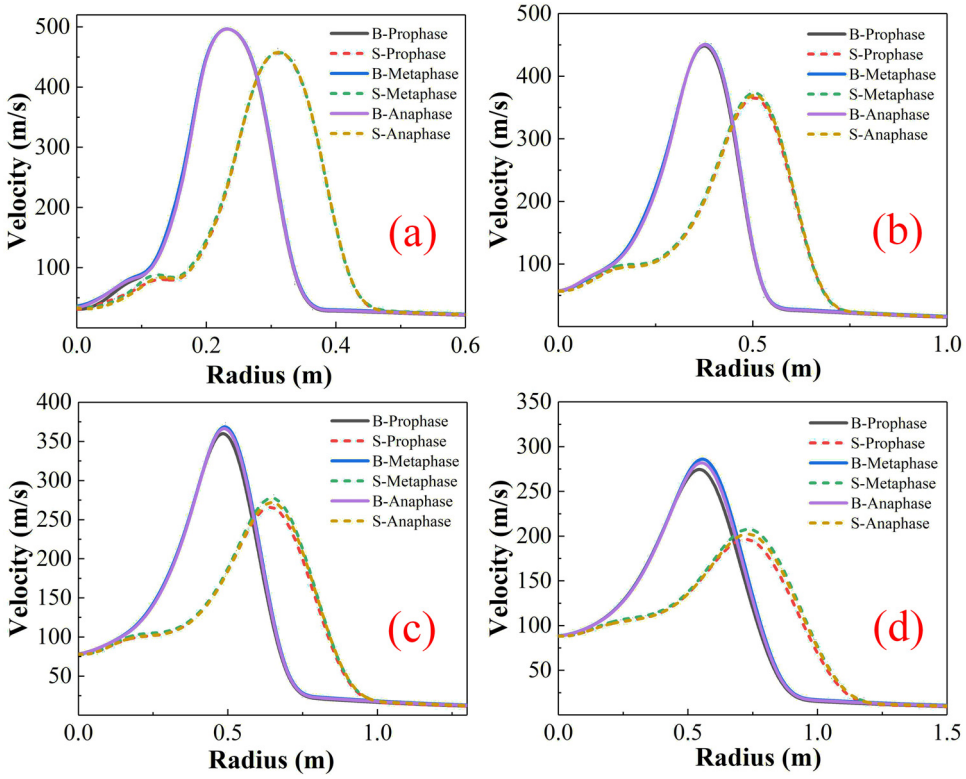

Figure 11: Radial velocity distribution of the jet under different atmospheric conditions: (a) 600 mm, (b) 1,300 mm, (c) 2,000 mm, and (d) 2,700 mm.

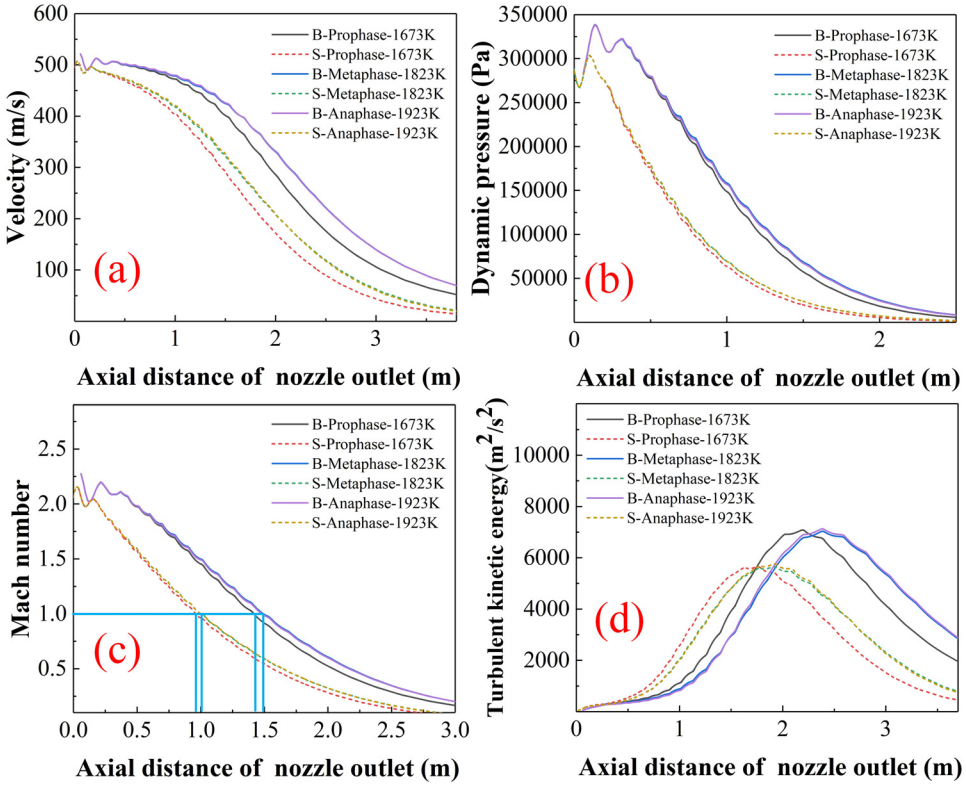

Figure 12: Jet characteristics of the nozzle axis for different smelting periods: (a) velocity, (b) dynamic pressure, (c) Mach number, and (d) turbulent kinetic energy.

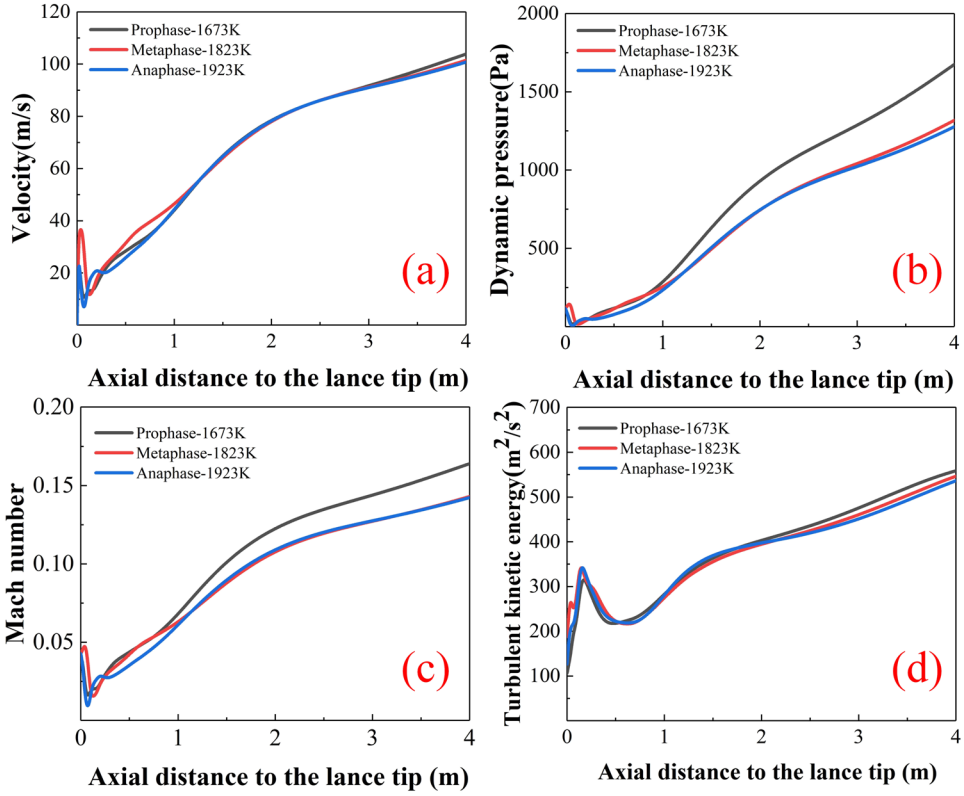

Figure 13: Jet characteristics of the nozzle centerline for different smelting periods: (a) velocity, (b) dynamic pressure, (c) Mach number, and (d) turbulent kinetic energy.

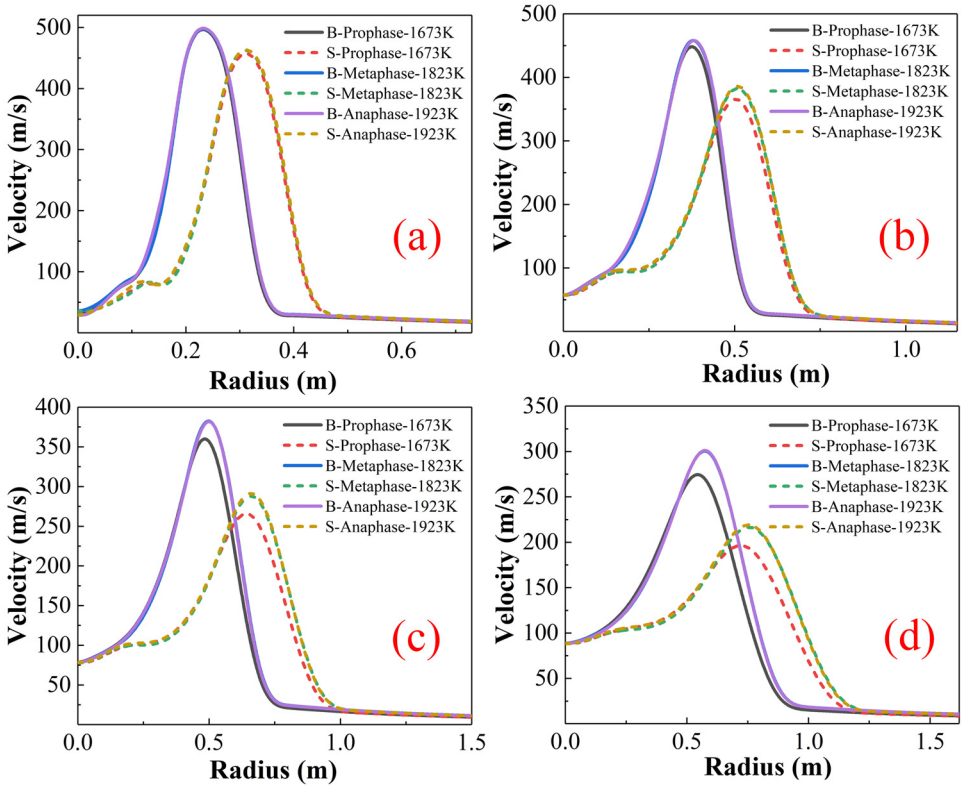

Figure 14: Distribution of the jet radial velocity for different smelting periods: (a) 600 mm, (b) 1,300 mm, (c) 2,000 mm, and (d) 2,700 mm.

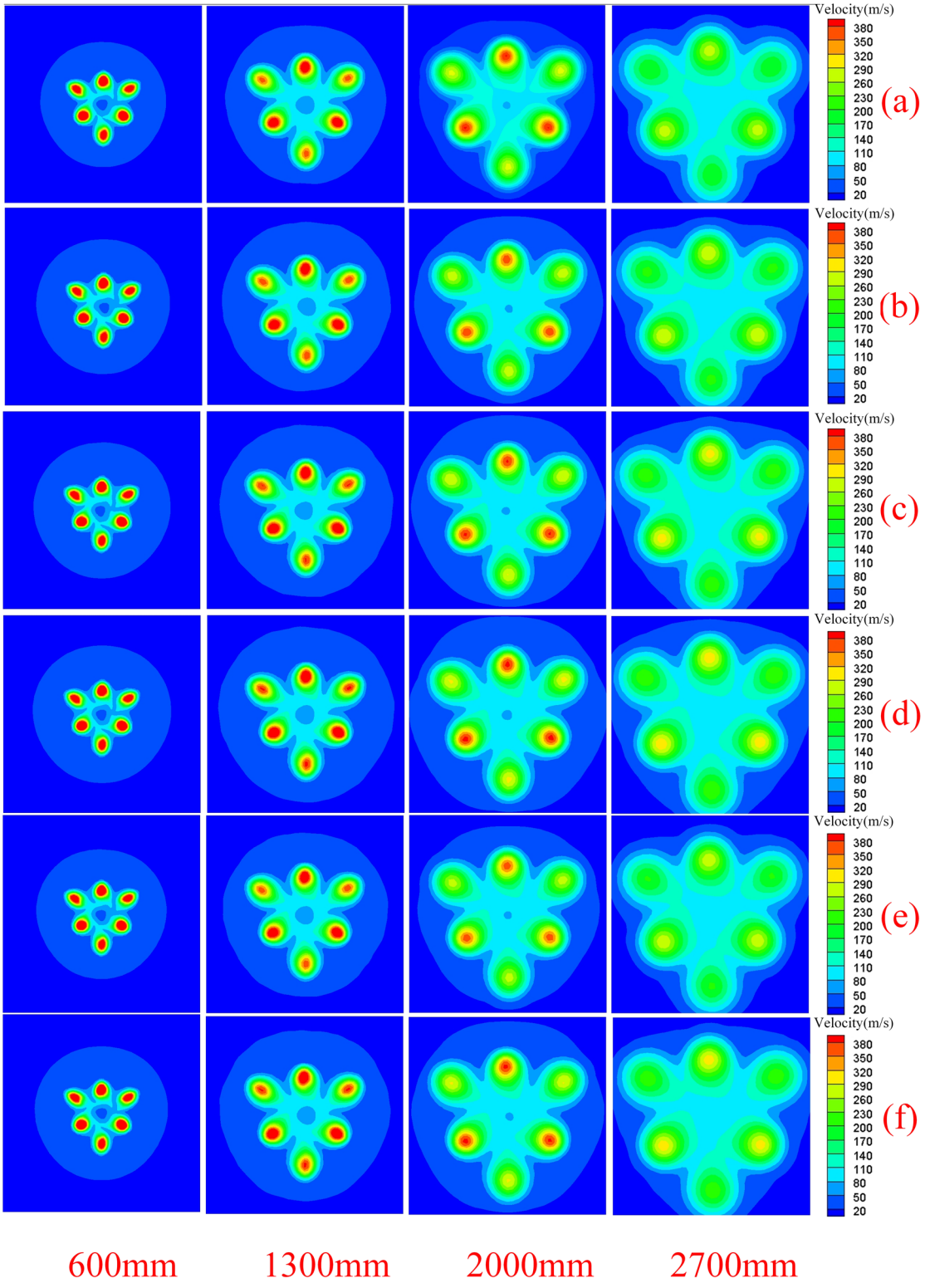

Figure 15: Distribution of the jet velocity field: (a) prophase 1,673 K, (b) metaphase 1,673 K, (c) metaphase 1,823 K, (d) metaphase 1,923 K, (e) anaphase 1,673 K, and (f) anaphase 1,923 K.

and the higher temperature in the converter in the later stage of smelting are conducive to slowing down the jet velocity attenuation and slowing down the jet axis offset.

Figure 15 shows the jet impingement area at different injection positions under different conditions. The results indicate that with the increase in the injection distance, the impact area of the jet increases. Under the same injection distance, the impact area of the jet increases with the increases in the CO concentration in the furnace gas and the ambient temperature. The results of Figure 15(a), (c), and (f) indicate that the jet impingement area and velocity field distribution are similar in the middle and late stages of smelting. Compared with the middle and late stages of smelting, the jet impingement area decreases in the early stage of smelting, and the jet mixing is more prominent with the increase in the injection distance. The results shown in Figure 15(a), (b), and (e) also show that under the same ambient temperature, the increase in the CO concentration in the furnace gas is conducive to increasing the impact area of the jet. The results shown in Figure 15(b), (c), and (d) also show that the impact area of the jet increases with the increase in ambient temperature under the same furnace gas composition. The results shown in Figure 15 can be explained based on Figures 12 and 14. The increase in CO concentration in the furnace gas and the increase in the ambient temperature in the converter are beneficial to increase the jet velocity and slow down the shift of the jet axis velocity. Therefore, the impact area of the jet increases with the increases in CO concentration in the furnace gas and the ambient temperature.

5 Conclusions

We simulated and analyzed the influence of gas composition and ambient temperature on the jet characteristics of a dual-parameter oxygen lance nozzle in the early, middle, and late stages of converter smelting when a CO_2–O_2 mixed injection was employed. We analyzed the jet characteristics, jet radial distribution, and characteristics of the oxygen lance nozzle outlet axis under the following conditions: identical gas compositions, different ambient temperatures, different gas compositions with identical ambient temperatures, and different smelting periods. The conclusions of the study are summarized as follows:

(1) Under the condition involving identical gas compositions, an increase in the ambient temperature causes a decrease in the attenuation rate of jet velocity and offset of the jet axis.
(2) At identical ambient temperatures, an increase in the CO concentration in the furnace gas leads to an elongation of the core section of the jet, slows down the attenuation of jet velocity, and weakens the coalescence degree of multiple jets.
(3) A higher CO concentration in the furnace gas in the middle stage of smelting and a higher ambient temperature in the late stage as compared to the early stage of smelting help slow down the attenuation of jet velocity.

Based on the results of this study, we conclude that the influence of the atmosphere and ambient temperature on jet characteristics should be considered when designing a dual-parameter mixed injection CO_2–O_2 nozzle. Furthermore, based on our results with the results from theoretical research, we conclude that the position of the oxygen lance should be adjusted appropriately to meet the smelting requirements in practical applications. We only simulated the jet characteristics of three different furnace gas compositions because the furnace gas composition changes in real time in the process of converter smelting. An analysis of the jet characteristics in different stages of converter smelting, especially at the beginning and the end of blowing, constitutes the future scope of this study.

Funding information: This work was supported by the National Natural Science Foundation of China (No. 52004023), the Fundamental Research Funds for the Central Universities (FRF-TP-19-031A1).

Author contributions: Chao Feng: Conceptualization, writing – original draft; Rong Zhu: methodology; Guangsheng Wei: writing – review & editing; Jianfeng Dong: validation; and Kai Dong: project administration.

Conflict of interest: Authors state no conflict of interest.

References

[1] Wang, M. L. and W. Y. Yang. Dephosphorization in the early stage of converter steelmaking. *Ironmaking and Steelmaking*, Vol. 6, 2019, pp. 1127–1134.
[2] Miyata, M., T. Tamura, and Y. Higuchi. Development of hot metal dephosphorization with lime powder top blowing: part 2. high blowing rate. *ISIJ International*, Vol. 57, No. 10, 2017, pp. 1756–1761.

[3] Li, Q., M. M. Li, S. B. Kuang, and Z. S. Zou. Numerical simulation of the interaction between supersonic oxygen jets and molten slag–metal bath in steelmaking of process. *Metallurgical and Materials Transactions B: Process Metallurgy and Materials Processing Science*, Vol. 46, 2015, pp. 1494–1509.

[4] Wang, W. J., Z. F. Yuan, H. Matsuura, H. X. Zhao, C. Dai, and F. Tsukihashi. Three-dimensional compressible flow simulation of top-blown multiple jets in converter. *ISIJ International*, Vol. 50, 2010, pp. 491–500.

[5] Sun, Y. H., X. T. Liang, J. H. Zeng, J. Chen, and L. Chen. Numerical simulation and application of oxygen lance in 120t BOF of PANSTEEL. *Ironmaking and Steelmaking*, Vol. 44, 2016, pp. 76–80.

[6] Wei, X., R. Zhu, L. Liu, D. Zhang, and C. Yang. Numerical simulation of oxygen lance jet in 100t converter. *Steelmaking*, Vol. 27, 2020, pp. 28–30.

[7] Liu, F., D. Sun, R. Zhu, and J. Ke. Effect of nozzle twisted oxygen lance on flow field and dephosphorisation rate in converter steelmaking process. *Ironmaking and Steelmaking*, Vol. 44, 2016, pp. 640–648.

[8] Wang, M. L., Y. H. Lv, W. Y. Yang, S. G. Li, and X. W. Xu. Selection of oxygen pressure in BOF steelmaking. *Journal of Iron and Steel Research International*, Vol. 18, 2011, pp. 12–16.

[9] Garajau, F. S., M. De Souza, L. Guerra, B. T. Maiaa, P. R. Cetlinb, and D. A. Moreira. Case study: wear in supersonic nozzle of tip lance in vallourec brazil steelmaking. *AISTech 2017 Proceedings*, 2017, p. 1365.

[10] Lv, M. and R. Zhu. Research on coherent jet oxygen lance in BOF steelmaking process. *Metallurgical Research and Technology*, Vol. 116, 2019, id. 502.

[11] Li, M. M., Q. Li, S. B. Kuang, and Z. S. Zou. Coalescence characteristics of supersonic jets from multi-nozzle oxygen lance in steelmaking BOF. *Steel Research in International*, Vol. 86, 2015, pp. 1517–1529.

[12] Zhang, B., K. Chen, R. F. Wang, C. J. Liu, and M. F. Jiang. Physical modelling of splashing triggered by the gas jet of an oxygen lance in a converter. *Metals*, Vol. 9, 2019, id. 409.

[13] Liu, F. H., D. B. Sun, R. Zhu, and Y. L. Li. Characteristics of flow field for supersonic oxygen multijets with various laval nozzle structures. *Metallurgical and Materials Transactions B: Process Metallurgy and Materials Processing Science*, Vol. 50, 2019, pp. 2362–2376.

[14] Hu, S. Y., R. Zhu, K. Dong, and G. S. Wei. Effect of oxygen flow rate and temperature on supersonic jet characteristics and fluid flow in an EAF molten bath. *Canadian Metallurgical Quarterly*, Vol. 57, 2017, pp. 219–234.

[15] Yang, L. Z., Z. S. Yang, G. S. Wei, Y. F. Guo, F. Chen, and F. Q. Zhang. Influence of ambient and oxygen temperatures on fluid flow characteristics considering swirl-type supersonic oxygen jets. *ISIJ International*, Vol. 59, 2019, pp. 2272–2282.

[16] Alam, M., J. Naser, and G. Brooks. Computational fluid dynamics simulation of supersonic oxygen jet behavior at steelmaking temperature. *Metallurgical and Materials Transactions B: Process Metallurgy and Materials Processing Science*, Vol. 41, 2010, pp. 636–645.

[17] Wei, G., R. Zhu, T. Cheng, and F. Zhao. Numerical simulation of jet behavior and impingement characteristics of preheating shrouded supersonic jets. *Journal of Iron and Steel Research International*, Vol. 23, 2016, pp. 997–1006.

[18] Garajau, F. S., M. S. Guerra, B. T. Maiaa, and P. R. Cetlinb. Effects of post combustion temperature on the wear of the supersonic nozzles in BOF lance tip. *Engineering Failure Analysis*, Vol. 96, 2019, pp. 175–185.

[19] Yang, W. Y., C. Feng, M. L. Wang, Y. H. Lv, Y. B. Hu, and X. Y. Peng. Water model experiment of high supplying oxygen blowing in large converter. *Journal of Iron and Steel Research International*, Vol. 29, 2017, pp. 807–815.

[20] Zhao, F., R. Zhu, and W. R. Wang. Characteristics of the supersonic combustion coherent jet for electric arc furnace steelmaking. *Materials*, Vol. 12, No. 21, 2019, id. 3504.

[21] Han, B. C., G. S. Wei, R. Zhu, W. H. Wu, J. J. Jiang, C. Feng, et al. Utilization of carbon dioxide injection in BOF–RH steelmaking process. *Journal of CO_2 Utilization*, Vol. 34, 2019, pp. 53–62.

[22] Yin, Z., R. Zhu, B. Chen, C. Wang, and J. Ke. Fundamental research on controlling BOF dust by COMI steel-making process. *Ironmaking and Steelmaking*, Vol. 44, 2009, pp. 92–94.

[23] Bi, X., R. Zhu, R. Liu, M. Lv, and C. Yi. Fundamental research on CO_2 and O_2 mixed injection stainless steelmaking process. *Steelmaking*, Vol. 28, 2012, pp. 67–70.

[24] Lv, M., R. Zhu, X. Y. Wei, H. Wang, and X. R. Bi. Research on top and bottom mixed blowing CO_2 in converter steelmaking process. *Steel Research International*, Vol. 83, 2012, pp. 11–15.

[25] Lv, M., R. Zhu, and L. Z. Yang. High efficiency dephosphorization by mixed injection during steelmaking process. *Steel Research International*, Vol. 90, No. 3, 2018, id. 1800454.

[26] Li, M. M., L. Li, B. Zhang, Q. Li, W. Wu, and Z. S. Zou. Numerical analysis of the particle-induced effect on gas flow in a supersonic powder-laden oxygen jet. *Volume*, Vol. 51, 2020, pp. 1718–1730.

[27] Yao, L. J., R. Zhu, Y. X. Tang, G. S. Wei, and K. Dong. Effect of furnace gas composition on characteristics of supersonic oxygen jets in the converter steelmaking process. *Materials*, Vol. 13, No. 15, 2020, id. 3353.

[28] Cuoci, A., A. Frassoldati, T. Faravelli, and E. Ranzi. Fluid dynamics and kinetic aspects of syngas combustion. In *29th Meeting of the Italian Section of The Combustion Institute*, 2006, pp. IV6-1–IV6-6.

[29] Aminian, J., J. C. Galletti, S. Shahhosseini, and L. Tognotti. Numerical investigation of a MILD combustion burner: analysis of mixing field, chemical kinetics and turbulence-chemistry interaction. *Flow, Turbulence and Combustion*, Vol. 88, 2012, pp. 597–623.